

# **Phases of $\text{Na}_x\text{CoO}_2$**

**by**

**Aakash Pushp**

**(pushp@uiuc.edu)**

## **Abstract**

This paper deals with the various phases of  $\text{Na}_x\text{CoO}_2$  ranging from charge ordered insulator to Curie-Weiss metal to superconductor as the stoichiometry is changed and attempts to understand the related theory and experimental results.

It starts with investigating the superconducting properties of this material, intercalated with  $\text{H}_2\text{O}$  and goes on to describe the various phases that come into being as  $x$  is varied. It then concentrates on another remarkable phase at  $x = \frac{1}{2}$  which is an insulator. For all other doping, this material shows metallic behavior. Later, it tries to give a clear account of the various experiments performed including ARPES and discusses its anisotropic hole-type large hexagonal-like Fermi surface and its implications.

## Introduction

Since the discovery of high- $T_c$  superconductivity in layered copper oxides, many other metal oxides involving 3d-transition metals, such as cobalt and nickel, have been investigated for similar behavior. Such attempts have normally failed but in March 2003 Takada *et al.* [1] reported that  $\text{Na}_x\text{CoO}_2 \cdot y\text{H}_2\text{O}$  ( $x \sim 0.35$ ,  $y \sim 1.3$ ) is a superconductor with a  $T_c$  of about 5 K. This compound consists of 2-dimensional  $\text{CoO}_2$  separated by a thick insulating layer of  $\text{Na}^+$  ions and  $\text{H}_2\text{O}$  molecules. It shows a marked resemblance in the superconducting properties with high- $T_c$  copper oxides, suggesting that both the systems have similar underlying physics.

## X-Ray Diffraction data

Takada *et al.* [1] obtained  $\text{Na}_x\text{CoO}_2 \cdot y\text{H}_2\text{O}$  sample through chemical oxidation of the parent compound  $\text{Na}_{0.7}\text{CoO}_2$  [4]. Before oxidation,  $\text{Na}_{0.7}\text{CoO}_2$  has a hexagonal layered structure (space group  $P6_3/mmc$ ) consisting of the 2D layers of  $\text{CoO}_2$  and charge balancing  $\text{Na}^+$  ions (Figure 1). Figure 2 shows an XRD pattern of the product obtained from oxidation. All the reflections were index matched on the basis of space

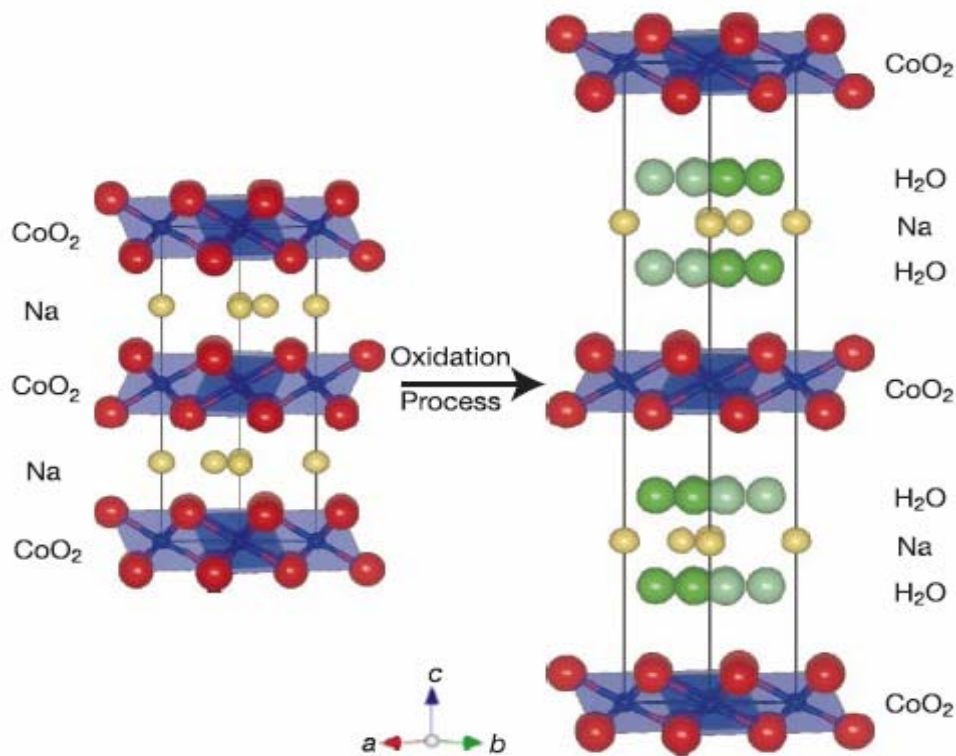


Figure 1: Structural views of  $\text{Na}_{0.7}\text{CoO}_2$  (left) and  $\text{Na}_x\text{CoO}_2 \cdot y\text{H}_2\text{O}$  (right), where Na and  $\text{H}_2\text{O}$  sites are partially occupied. [ref. 1]

group  $P6_3/mmc$ . A marked increase in  $c$  was observed supporting the idea that the intercalation of certain ‘guest’ molecules occurred in the oxidation process in addition to the de-intercalation of  $\text{Na}^+$  ions.  $\text{H}_2\text{O}$  is the most probable candidate for the guest molecule. The composition calculated by inductively coupled plasma atomic-emission spectroscopy (ICP-AES) based on this assumption was  $\text{Na}_{0.35}\text{CoO}_2 \cdot 1.3\text{H}_2\text{O}$ . Further, infrared spectroscopy showed that the  $\text{H}_2\text{O}$  content was 1.24 per formula unit.

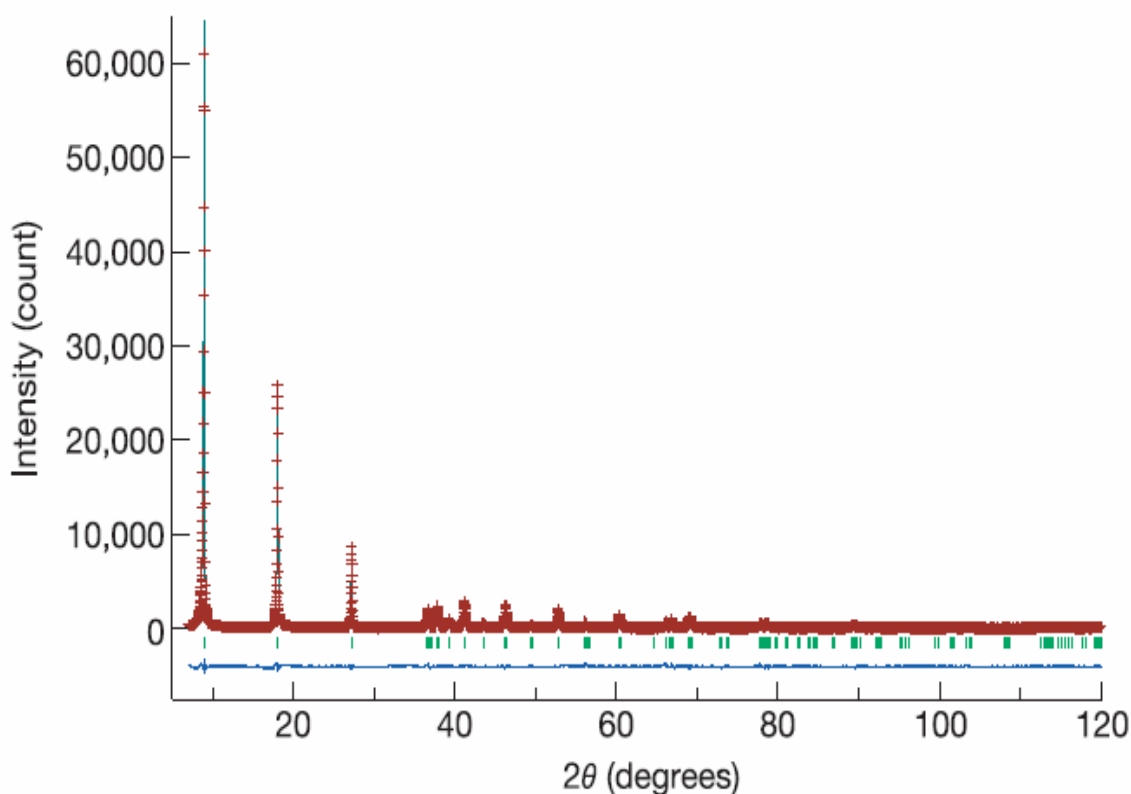


Figure 2: Rietveld refinement patterns for  $\text{Na}_x\text{CoO}_2 \cdot y\text{H}_2\text{O}$ . The observed diffraction intensities are represented by red plus signs, and the calculated pattern by the green solid line. Short light green vertical bars below the observed and calculated patterns indicate the positions of allowed Bragg reflections. The oxidation process slightly decreased  $a$  from 2.8292(3) Å for the parent compound to 2.8230(2) Å, where the parentheses indicate standard deviations, probably because  $\text{Co}^{3+}$  ions were partially oxidized to smaller  $\text{Co}^{4+}$  ions. On the other hand,  $c$  increased dramatically from 10.9628(8) Å to 19.6207(14) Å. [ref. 1]

Rietveld analysis of the XRD data was carried out adopting a structural model shown in the right side of Figure 1. In this model,  $\text{H}_2\text{O}$  molecules are located at  $12k$  sites on the basis of electron-density distribution obtained by a maximum-entropy method. The Rietveld refinement patterns are shown in Figure 2. The  $\text{H}_2\text{O}$  content resulting from these analyses came out to be 1.47 per formula unit, which is close to analytical values.

## Magnetic Susceptibility and resistivity

The magnetic susceptibility of  $\text{Na}_x\text{CoO}_2 \cdot y\text{H}_2\text{O}$  is plotted in Fig. 3 as a function of temperature. A steep decrease of susceptibility is observed in the measurements under the magnetic field  $H = 20$  Oe at about 5 K both in zero-field cool (ZFC) and field cool (FC) processes.

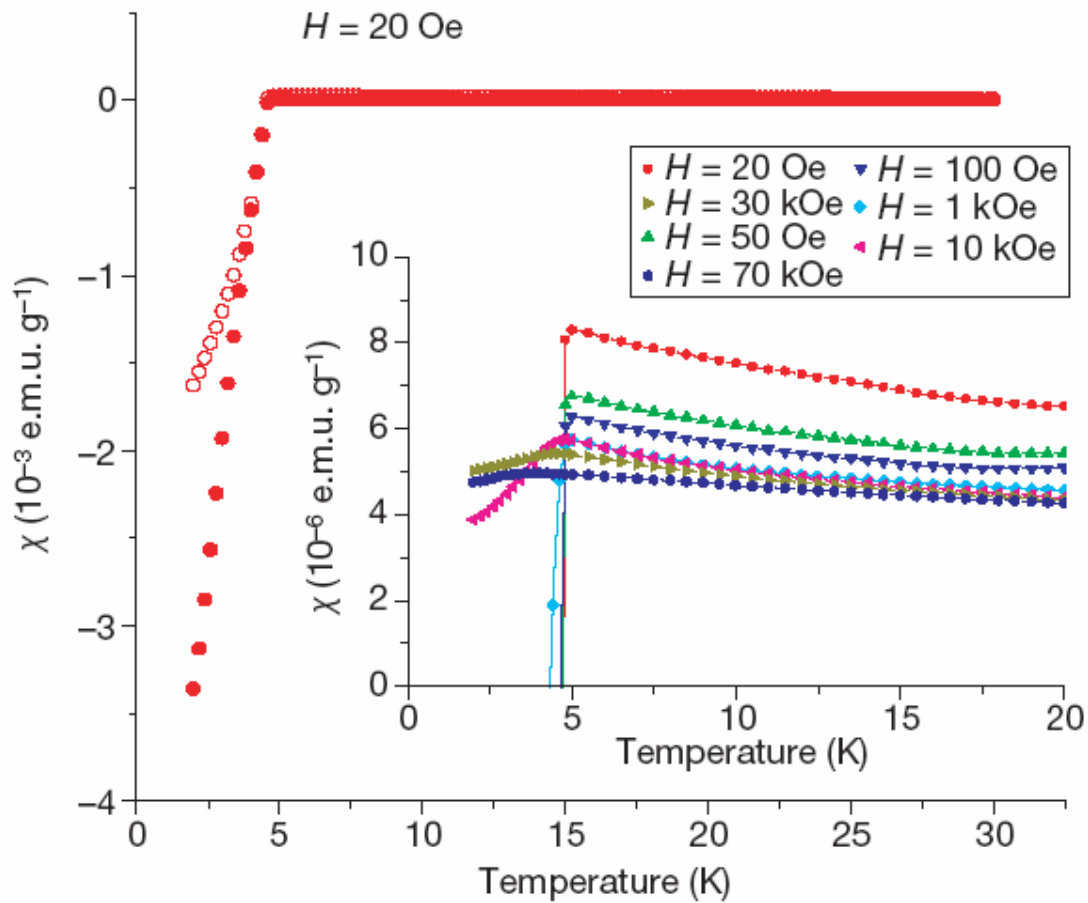


Figure 3: Magnetic susceptibility ( $\chi$ ) of  $\text{Na}_x\text{CoO}_2 \cdot y\text{H}_2\text{O}$ . Filled circles, zero-field cooling; open circles, field cooling. The susceptibility was measured in a magnetic field of 20 Oe. The inset shows  $\chi$  measured under various magnetic fields by the zero-field cooling process. [ref. 1]

From the susceptibility data, it can be concluded that the present phase undergoes superconducting transition at about 5 K, because only superconductivity can account for such a large diamagnetism. Downturn of the susceptibility was still observed near 5 K even at 70 kOe, but the transition became quite broad and the susceptibility was not negative even at 2 K.

The electric resistivity ( $\rho$ ) of  $\text{Na}_x\text{CoO}_2 \cdot y\text{H}_2\text{O}$  is shown in Fig. 4. Zero resistivity was not obtained down to 2 K in sample made by Takada *et al.* [1] because it was impossible to prepare a tightly sintered ceramic specimen.

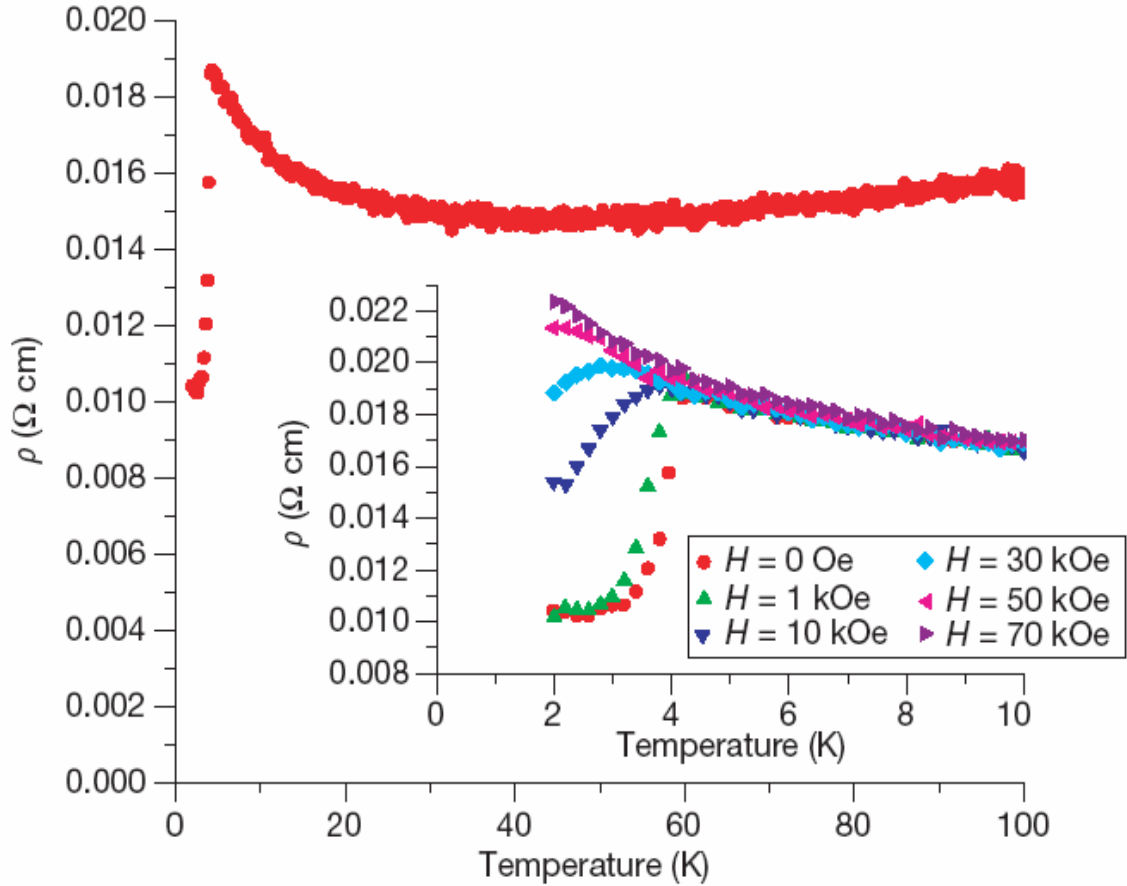


Figure 4: Resistivity ( $\rho$ ) of  $\text{Na}_x\text{CoO}_2 \cdot y\text{H}_2\text{O}$  under zero magnetic field. The inset figure shows the resistivity measured under various magnetic fields. [ref. 1]

Nevertheless, a sharp decrease of resistivity can be seen at around 4 K, supporting the superconducting transition. The onset temperature is lower in resistivity measurement than that of the susceptibility measurement because of variation of water content in the sample.

The behavior of this material not only depends on the water content but also on the Na content. The phase change of this material ranges from that of a paramagnetic metal ( $x \sim 0.3$ ) to a charge-ordered insulator (at  $x = 0.5$ ) to a Curie-Weiss metal ( $x \sim 0.7$ ), and finally to a weak-moment magnetically ordered state ( $x > 0.75$ ). The next section discusses the various phases of  $\text{Na}_x\text{CoO}_2$ .

## Phases of $\text{Na}_x\text{CoO}_2$

Research on oxide conductors has uncovered many interesting electronic states characterized by strong interaction, which include superconductivity, and charge or spin ordered states [5, 6].  $\text{Na}_x\text{CoO}_2$  is one such oxide. At the doping  $x \sim 2/3$ ,  $\text{Na}_x\text{CoO}_2$  exhibits an unusually large thermopower [7]. Although  $\text{Na}_x\text{CoO}_2$  shows metallic resistivity, its magnetic susceptibility shows a surprising Curie-Weiss profile [8], and its magnitude is comparable with that of antiferromagnetically coupled spin-1/2 local moments equal in number to the hole carriers [9]. Another interesting observation is that the thermopower at 2.5 K gets suppressed by an in-plane magnetic field [9], which implies that the enhanced thermopower is largely due to spin entropy carried by strongly correlated holes ( $\text{Co}^{4+}$  sites) hopping on the triangular lattice. We have already seen in the previous section that when intercalated with water,  $\text{Na}_x\text{CoO}_2 \cdot y\text{H}_2\text{O}$  becomes superconducting for  $1/4 < x < 1/3$  [10, 11, 12]. In order to find out if the Curie-Weiss state at  $2/3$  is continuous with the  $1/3$  state surrounding superconductivity, and if charge-ordering effects are important, Cava *et al.* [2] have completed a phase diagram of non-hydrated  $\text{Na}_x\text{CoO}_2$ . The phase diagram depicts a variety of electronic states as  $x$  is increased from 0.3 to 0.75. One of the most interesting among them is at  $x = 1/2$  that involves charge ordering of the holes together with the  $\text{Na}^+$  ions.

## Experimental details

Cava *et al.* [2] accurately measured the variation of the  $c$ -axis lattice parameter variation as  $x$  is increased (Figure 5C). Figure 5A shows magnetic susceptibility  $\chi$  vs.  $T$  as  $x$  is varied. For  $x \sim 2/3$ ,  $\chi$  vs.  $T$  follows the Curie-Weiss law  $\chi = C/(T + \theta)$  with  $\theta \sim 70$  K. Above  $2/3$ , at  $x = 0.75$ ,  $\chi$  is slightly rounded below 20 K, consistent with the appearance of a weak magnetization  $M$ . For  $x > 3/4$ , a spin-density-wave (SDW) has been suggested [13, 14]. When  $x$  is decreased below  $2/3$ , the Curie-Weiss divergence in  $\chi$  gets progressively reduced until it vanishes at  $x = 1/2$ . At  $x = 1/2$ ,  $\chi$  reveals two sharp cusps at  $T_{c1} = 88$  K and  $T_{c2} = 53$  K, which signal the onset of an insulating state. With further decrease of  $x$  below  $1/2$  to  $x = 0.31$ , the  $\chi$  plot becomes featureless, but its magnitude remains large as compared with the Pauli susceptibility in conventional metals.

The in-plane resistivity  $\rho$  shows a dramatic change in behavior across  $x = 1/2$  (Figure 5B).  $\text{Na}_x\text{CoO}_2$  is metallic in its  $T$  dependence at all values away from  $x = 1/2$ . Insulating behavior abruptly appears at  $x = 1/2$ , in contrast to the metallic states at all other values of  $x$ . Initially, as the temperature is lowered towards  $T_{c1}$  and  $T_{c2}$ , the resistivity increases gradually. Below  $T_{c2}$ , however,  $\rho$  shoots up rapidly. At lower doping ( $x = 0.31$ ), it behaves as a high-conductivity metallic state. Below 30 K,  $\rho$  follows a  $T^2$  behavior and falls down to a value almost 5 times lower than at  $x = 0.71$ .

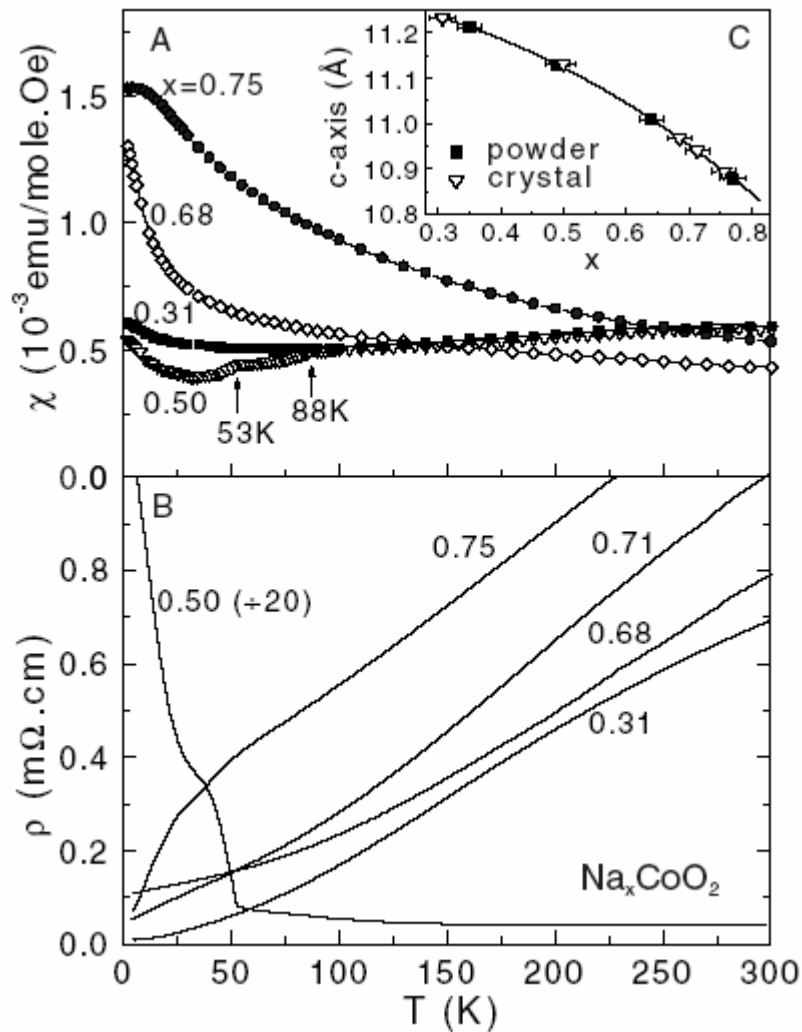


Figure 5: The susceptibility  $\chi$  (A) and in-plane resistivity  $\rho$  (B) of single crystals of  $\text{Na}_x\text{CoO}_2$  with  $x$  determined by ICP (C). In Panel A,  $\chi$  is measured in an in-plane field  $H = 5$  T. In the crystal with  $x = 0.75$ ,  $\chi$  fits the Curie-Weiss form  $\chi = C/(T + \theta)$  (with  $\theta \sim 150$  K and  $C = 2.81$  cm<sup>3</sup>K/mole). For  $x = 0.5$ , sharp transitions are observed at  $T_{c1}$  and  $T_{c2}$  (arrows). Panel B shows the  $T$  dependence of  $\rho$  at selected  $x$ . Insulating behavior is observed at  $x = 0.5$  (data displayed at lower scale) in contrast to metallic behavior in the rest. At low  $T$ ,  $\rho$  is  $T$ -linear for  $x = 0.71$  but varies as  $T^2$  for  $x = 0.3$ . In Panel C, the  $c$ -axis lattice parameter measured by XRD is plotted against the Na content  $x$  fixed by ICP in powder samples. [ref. 2]

The susceptibility and resistivity measurements imply a phase diagram as shown in Figure 6. The interesting feature in the phase diagram is the narrow insulating state at  $x = \frac{1}{2}$  separating two distinct metallic states. It behaves as a paramagnetic material below  $x = \frac{1}{2}$  while shows a Curie-Weiss metallic state behavior above  $x = \frac{1}{2}$ .

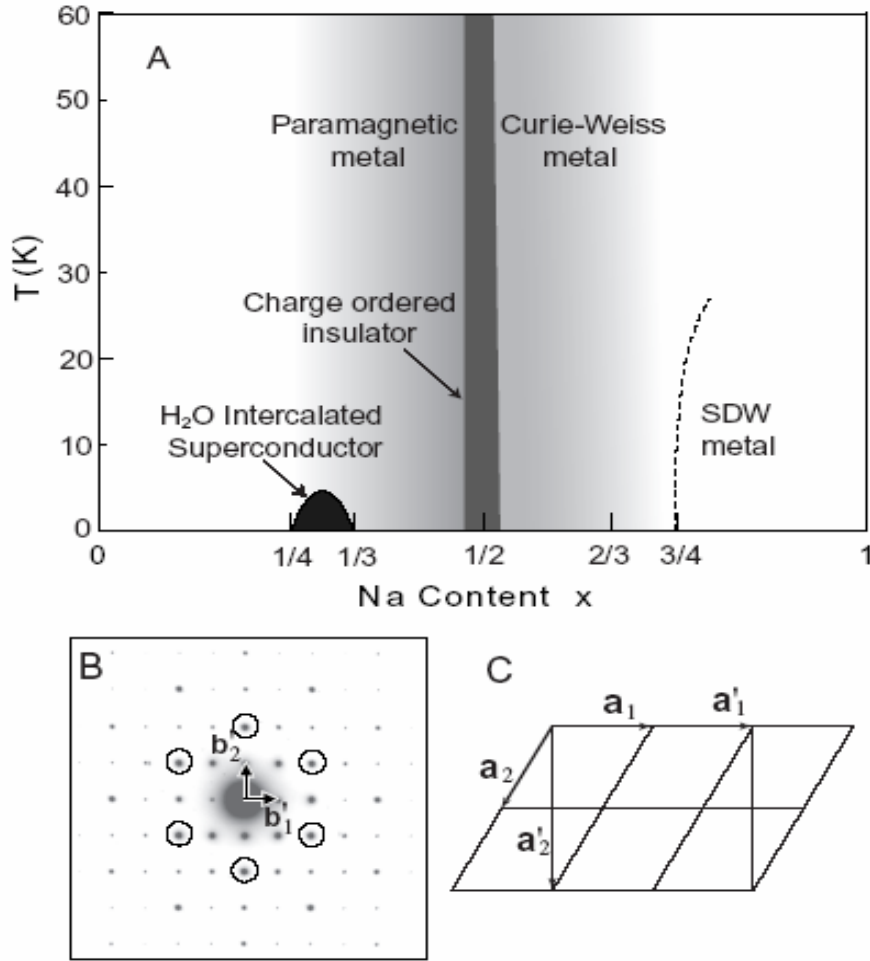


Figure 6: The phase diagram of non-hydrated  $\text{Na}_x\text{CoO}_2$  (A), electron diffraction pattern of a crystal with  $x = \frac{1}{2}$  (B) and the Na superstructure lattice (C). In Panel A, the charge-ordered insulating state at  $\frac{1}{2}$  is sandwiched between the paramagnetic metal at 0.3 and the Curie-Weiss metallic state at 0.65-0.75. The superconducting state is obtained on intercalation with  $\text{H}_2\text{O}$  [1, 10]. In Panel B, the diffraction pattern is taken along [001]. Bragg spots of the hexagonal lattice are circled. The spots located at  $n_1\mathbf{b}_1' + n_2\mathbf{b}_2'$  correspond to the supercell with lattice vectors  $\mathbf{a}_1'$  and  $\mathbf{a}_2'$  drawn in Panel C. [ref. 2]

Electron-diffraction (Figure 6B) reveals a very important feature of this interesting state at  $x = \frac{1}{2}$ . Even at 300 K, the Na ions order as a superstructure with lattice vectors  $\sqrt{3}a \mathbf{x}$  and  $2a \mathbf{y}$  (where  $a$  is the hexagonal parameter) as seen in the Bragg spots. At other doping levels, the superstructure Bragg spots are either much weaker or absent.

The thermal conductivity  $\kappa$  measured parallel to the layers also clearly depicts the long-range nature of the Na superstructure. As phonons are strongly scattered by disorder in the Na sublattice, the phonon mean free path  $l_{ph}$  is expected to be much longer for  $x = \frac{1}{2}$  due to the superstructure than at any other doping. This is confirmed by the data [2] of thermal conductivity  $\kappa$  vs.  $T$  for different doping (Figure 7).

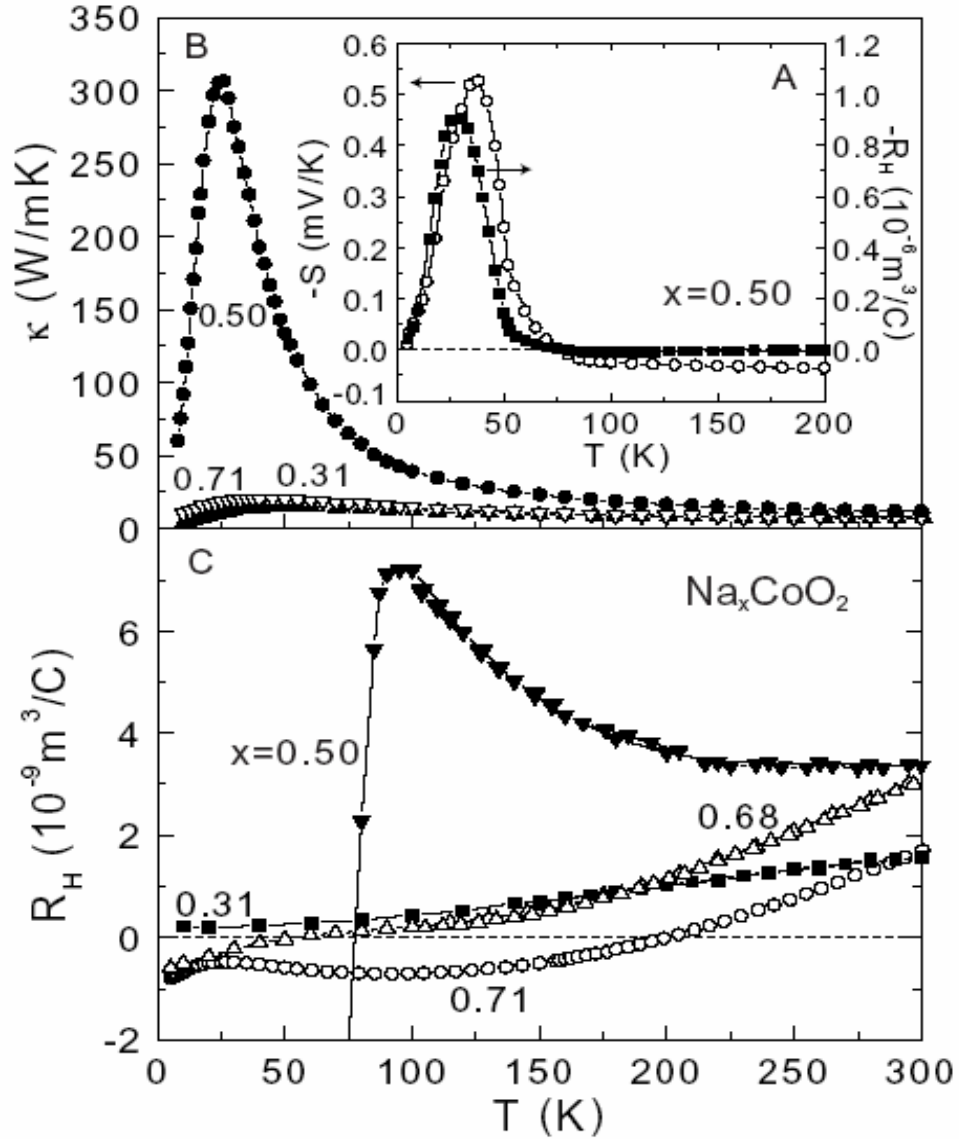


Figure 7: The thermopower  $S$  and the Hall coefficient  $R_H$  in  $\text{Na}_x\text{CoO}_2$  for  $x = 1/2$  (A), and plots of the in-plane thermal conductivity  $\kappa$  (B), and  $R_H$  (C) for several values of  $x$ . In Panel A, both  $|S|$  and  $|R_H|$  begin to increase steeply just below  $T_{c2}$  (88 K) and attain maxima at 40 and 30 K, respectively. Below the peak values, they fall towards zero as  $T \rightarrow 0$ , consistent with a particle-hole symmetric state. In Panel B,  $\kappa$  at  $x = 1/2$  rises to a very large peak value, whereas it remains small at all other  $x$ . Panel C shows that the curve of  $R_H$  vs.  $T$  at  $x = 1/2$  is qualitatively different from all other  $x$  values. In the metallic samples,  $R_H$  increases with  $T$ , consistent with strongly interacting carriers hopping on a triangular lattice. [ref. 2]

In the metallic samples ( $x = 0.31$  and  $0.71$ ),  $\kappa$  weakly depends on  $T$  and is also small in magnitude as compared to the  $\kappa$  for the  $x = 1/2$  sample.  $\kappa$  also shows a very steep rise near the  $T_{c2}$  confirming the superstructure lattice idea. Hence both the diffraction and  $\kappa$  results provide strong evidence that the Na ions at  $x = 1/2$ , unlike other metallic state, order with very long range correlation even at room temperature.

Even the Hall coefficient  $R_H$  at  $x = \frac{1}{2}$  shows a small peak before plunging down to large negative values. Above 200 K,  $R_H$  is hole-like with a  $T$ -independent value. Near  $T_{c1}$ ,  $R_H$  rises to a weak maximum and then plunges down to a large negative value. Below  $T_{c2}$ , it increases dramatically in magnitude to a peak value 250 times greater than its magnitude above 200 K. This giant increase in  $|R_H|$  indicates that the itinerant carrier density  $n$  decreases by  $\sim 2$  orders of magnitude. Once again, the corresponding plots for the metallic states are featureless. However,  $R_H$  in these metallic states is  $T$ -dependent above 200 K.

The behavior of  $R_H$  at low  $T$  has an unusual feature for the insulating state.  $|R_H|$  falls steeply towards zero as  $T \rightarrow 0$  as shown in Figure 7A. The usual behavior of semiconductors, for instance, is that it diverges as  $1/n$  (as  $n \rightarrow 0$ ). We know that in general,  $R_H = \sigma_H/H\sigma^2$ , where  $\sigma_H$  is the Hall conductivity and  $\sigma$  is the conductivity. The vanishing of Hall current at low temperature indicates that the charge excitations exhibit exact particle-hole symmetry, i.e., they are neither hole-like nor electron-like in their response to the applied magnetic field.

From the Angle-Resolved Photoemission (ARPES) data [3], a large hole-type hexagonal-like Fermi surface (FS) is observed. Figure 8 reveals a large hole-pocket centered around the  $\Gamma$ -point. The FS assumes a hexagonal character with an average radius of  $0.7 \pm 0.05 \text{ \AA}^{-1}$ . This is a bit larger than the size calculated for the related compound  $\text{Na}_{0.5}\text{CoO}_2$  using LDA, which may indicate that a fraction of the doped electrons are in the Fermi sea while the rest are presumably localized. The shape of the FS is rather hexagonal (anisotropic) in agreement with the LDA.

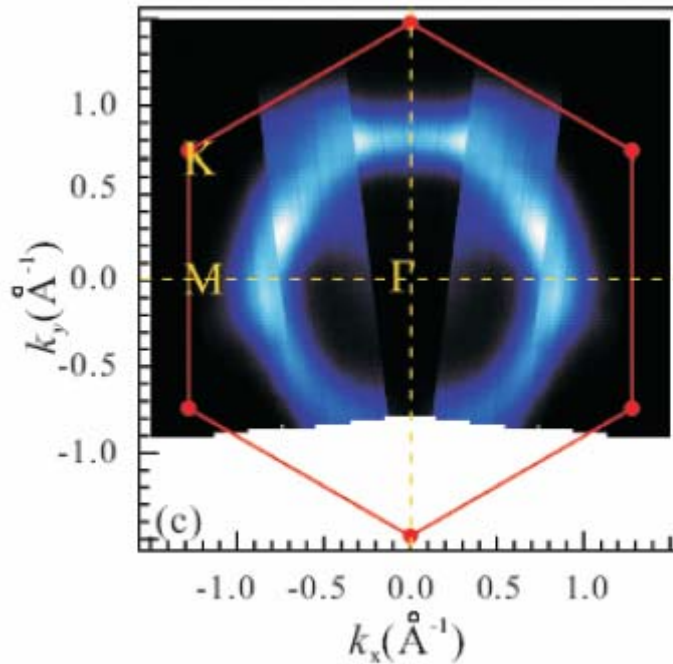


Figure 8: Fermi surface:  $n(k)$  plot generated by integrating within 75 meV of Fermi level. A large hole-pocket is centered around the  $\Gamma$ -point. The Fermi surface, exhibiting some hexagonal anisotropy, is the inner edge of pocket as shown over the complete Brillouin zone. [ref. 3]

Along the  $\Gamma \rightarrow M$  energy crossing the quasiparticle band crosses the Fermi level from M toward  $\Gamma$  (Fig. 9(a)) as opposed to  $\Gamma$  to M, which gives the single-particle hopping ( $t$ ) a negative sign. The total bandwidth of this system is estimated at 70(10) meV. For a tight binding hexagonal lattice total bandwidth  $W = 9t$  where  $t$  is the nearest neighbor single-particle hopping. Hence the effective nearest neighbor single particle hopping,  $t_{eff}$  in this system can be estimated to be about 8(2) meV. It is interesting to note that this value is on the order of the exchange coupling  $J$  ( $\sim 10$  meV) [8], which suggests that the charge motion would be significantly affected by the spin dynamics of the system.

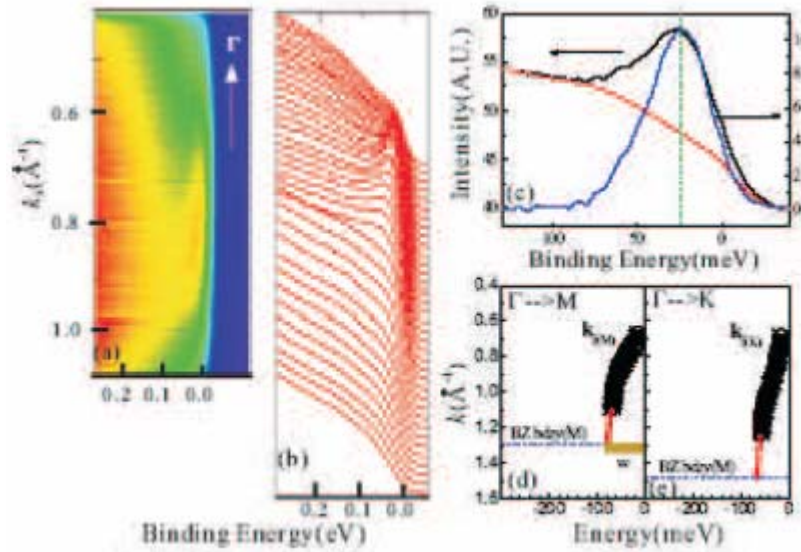


Figure 9: Quasiparticle dispersion: (a)  $\Gamma \rightarrow M$  Fermi crossing. Color red reflects the highest intensity - yellow to green to blue is in the order of decreasing intensity. (b) EDCs corresponding to the image plot in (a). (c) A single EDC for  $k = 0.78 \text{ \AA}^{-1}$ . To extract the peak position a background is subtracted. A constant step-like background is best seen in Fig 9(a). Based on the extracted peak positions  $E$  vs.  $k$  plots are made as shown in (d) for  $\Gamma \rightarrow M$  and in (e) for  $\Gamma \rightarrow K$  directions. [ref. 3]

The quasiparticle spectral weight near the Fermi level as a function of temperature has been plotted in Figure 10. It is interesting to note that the quasiparticle weight decreases to almost zero on raising the temperature to around 120 K (Fig. 10(b)). This roughly coincides with the temperature region where the  $T$ -linear behavior in resistivity gives way to stronger  $T$ -dependence. In other words, quasiparticles exist in this system only in the temperature regime where resistivity is linear in  $T$  and transport behavior is non-Fermi liquid like, in stark contrast with the conventional expectation that well defined quasiparticles are signatures of good Fermi liquid behavior.

Further, a strong temperature dependence of the 0.7 eV feature in  $\text{Na}_{0.7}\text{CoO}_2$  is yet another signature of this system's strongly correlated behavior in addition to its highly flat band character which is typical of strong electron-electron correlation.

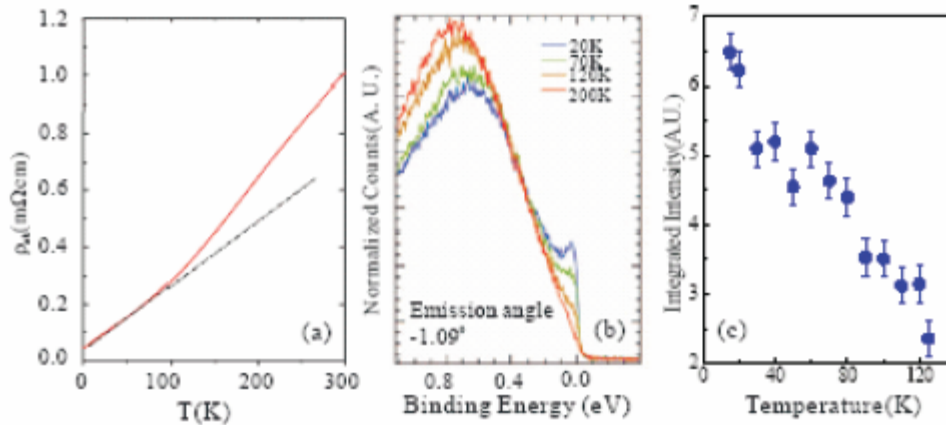


Figure 10: Temperature Dependence: (a) In-plane resistivity in  $\text{Na}_{0.7}\text{CoO}_2$  is linear up to 100 K [9] and then gradually crosses over to a stronger  $T$ -dependence. (b) Temperature dependence of quasiparticles near the  $\Gamma \rightarrow M$  Fermi crossing. The quasiparticle spectral weight ceases to exist above 120 K, close to the temperature where the  $T$ -linear behavior of the resistivity disappears. (c) Background subtracted integrated quasiparticle spectral weight is plotted as a function of temperature. [ref. 3]

## Conclusion

The phase diagram in Figure 6 reveals the strong influence of Na ion on the electronic properties of  $\text{Na}_x\text{CoO}_2$ . The insulating phase indicates a strong interaction between the ions and holes even though they occupy separate layers. For either charge species alone on the triangular lattice at  $x = 1/2$ , the liquid state seems to be more stable at finite temperature. If both populations are present, density fluctuations in one will strongly affect the other thereby giving interesting results in measurements of thermal conductivity, Hall coefficient, resistivity, magnetic susceptibility, etc. The superconducting state produced by intercalation with  $\text{H}_2\text{O}$  evolves from the paramagnetic metal which is separated from the Curie-Weiss state by the charge-ordered insulator. In other words, this system is a very good example of strongly interacting particles and is an interesting state of matter that offers rich Physics.

## Reference

- [1] K. Takada *et al.*, Nature **422**, 53 (2003)
- [2] M.L. Foo *et al.*, cond-mat/0312174
- [3] M.Z. Hasan *et al.*, cond-mat/0308438
- [4] C. Fouassier *et al.*, J. Solid State Chem. **6**, 532 (1973)
- [5] Y. Tokura, Physics Today **56**, 50 (2003).
- [6] A. P. Mackenzie, and Y. Maeno, Rev. Mod Phys. **75**, 657 (2003).
- [7] I. Terasaki *et al.*, Phys. Rev. B **56**, 12685 (1997).
- [8] R. Ray *et al.*, Phys. Rev. B **59**, 9454 (1999).
- [9] Y. Wang *et al.*, Nature **423**, 425 (2003).
- [10] R. E. Schaak *et al.*, Nature **424**, 527 (2003).
- [11] F. C. Chou *et al.*, cond-mat/0306659 (2003).
- [12] R. Jin *et al.*, Phys. Rev. Lett. **91**, 217001 (2003).
- [13] T. Motohashi *et al.*, Phys. Rev. B **67**, 064406 (2003).
- [14] J. Sugiyama *et al.*, cond-mat/0310516 (2003).